CRYSTAL GROWTH & DESIGN

pubs.acs.org/crystal

Article

Controlling CeO_2-(001) Film Surface Instability during Thermochemical Processing

L. Piperno,* A. Vannozzi, A. Mancini, R. B. Sonher, G. Sotgiu, and G. Celentano

Cite This: *Cryst. Growth Des.* 2025, 25, 3756−3766

Read Online

ACCESS | Metrics & More | Article Recommendations | Supporting Information

ABSTRACT: Cerium oxide (CeO_2) is a highly valuable material for various technological applications, particularly as a buffer layer in thin film deposition and epitaxial growth. In thin film technology, buffer layers such as CeO_2 are crucial to facilitate high-quality film growth on incompatible substrates, reducing lattice mismatch and minimizing defects during epitaxial growth. This is especially significant in high-performance superconducting devices known as coated conductors (CCs) that use CeO_2 buffer layers to ensure optimal performance. The quality of the buffer layer is vital, requiring (001)-oriented growth, layer continuity, and low roughness. This study explores (001)-oriented, CeO_2-based buffer layer growth via polymer-assisted deposition (PAD), assessing various methods to promote the exposure of the polar, highly unstable (001) surface, through a wide comparative analysis of different compositions and processing parameters backed with a theoretical explanation of the results. We show that processes such as thermal grooving/surface reconstruction can be controlled to obtain oriented, epitaxial films with low roughness values (<1 nm) and no porosity, suitable for their use as templates for the deposition of a superconducting layer.

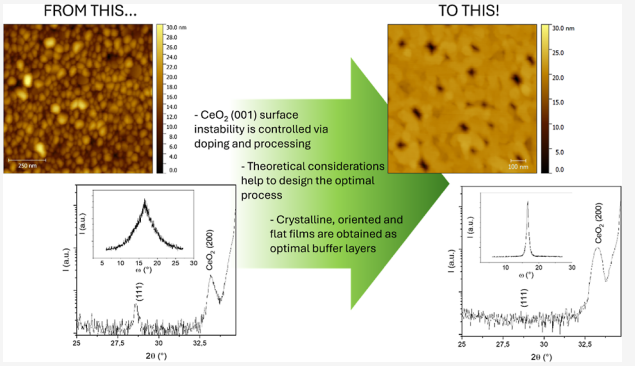

INTRODUCTION

Cerium oxide (CeO_2) is a rare earth metal oxide known for its versatility and its successful use in many different technological applications.[1−6] In particular, it is often employed as a buffer layer in the field of thin film deposition and epitaxial growth to promote the growth of high-quality films on substrates or multilayered structures that may not be naturally compatible.[7−12] Indeed, cerium oxide serves as an effective buffer layer due to its lattice structure, which is compatible with many functional materials, helping to reduce lattice mismatch and minimize defects during epitaxial growth. This is particularly important in the fabrication of the high-performance superconducting devices known as coated conductors (CCs).[13−20] CCs are advanced, multilayered devices based on high-temperature superconducting (HTS) materials or iron-based superconductors (IBSC) designed to carry large electrical currents with minimal losses. These conductors consist of a superconducting layer, typically made of yttrium barium copper oxide (YBCO), or the IBSC Fe(Se,Te), deposited on a flexible, metallic substrate[17,18,21−23] suitable for a wide range of applications, including power cables, fault current limiters, magnetic resonance imaging (MRI) systems, and large magnets for fusion applications.[24−27] The metallic substrate is usually coated with buffer layers, such as cerium oxide, to allow for the epitaxial growth of the superconducting film,[13] thus ensuring its best performances, and to protect it from diffusion of ions from the substrate.[28] In this scenario, it follows that the quality of the buffer layer is essential for the performance of the whole CC. In order to carry out its function, the main standards to be met by the buffer are oriented growth, continuity of the layer, and low roughness value. In this work, we want to develop a low-cost, chemical technique suitable for industrial scale-up for the growth of CeO_2 buffer layers, systematically exploring the process of CeO_2 growth on Y-stabilized-ZrO_2 single crystals (YSZ) via polymer-assisted deposition (PAD), a very versatile technique developed for the deposition of oxide thin films with low values of roughness[29−33] and of nanostructures.[31,34−36] Most importantly, with respect to other widely studied chemical solution deposition methods, PAD is preferred because of the use of water-based starting solutions, the high stability of the solutions in time, and the complete control over secondary reactions obtained through ion complexation with polymers.[29−31,35−38] The study starts from pure CeO_2 films and proceeds to evaluate the effects of different doping elements and deposition/growth conditions on the parameters men-

Received: February 11, 2025
Revised: May 5, 2025
Accepted: May 13, 2025
Published: May 19, 2025

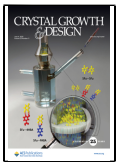

tioned above (orientation, morphology, roughness). Indeed, it will be shown how it is possible to tune the buffer layer surface morphology according to specific needs, by closely controlling the material processing, introducing different kinds of doping, and/or varying the growth conditions. With respect to the available literature on this topic, the less well-known method PAD is used, and a thorough comparative analysis is performed. The obtained results are interpreted with the aid of nucleation and growth theory, showing that different competitive phenomena occur during crystallization and how it is possible to control them. It should be noted that these results can be generalized to any chemical solution deposition method for ceria-based thin films, such as metal organic decomposition (MOD), sol−gel, etc., since the starting point for CeO_2 crystallization after decomposition of the organic precursors is the same Ce−O matrix, irrespective of the original Ce sources and solvents employed. This consideration is supported by the direct comparison of the morphologies obtained for this system that are comparable to those of CeO_2 films prepared with the other solution techniques mentioned before (MOD, sol−gel),[9] and also with physical techniques,[39,40] thus confirming the universal nature of the phenomena under discussion. It should be also stressed that the conclusions drawn in this paper for buffered single crystals are not limited to this kind of substrates, since it was proven that oxide buffer layers can be successfully grown on metallic templates at high temperatures (up to 1100 °C) in the appropriate atmosphere,[20,21] making PAD an appropriate technique to investigate in view of its application on larger scales.

EXPERIMENTAL METHODS

Preparation of the Buffer Layers via PAD. The deposition of CeO_2 films via PAD requires the preparation of metal−polymer aqueous solutions of Ce^{4+} (1.5 M): $Ce(Acetate)_4$ (99.9%, Sigma-Aldrich) was dissolved in 8 mL of ultrapure water together with ethylenediaminetetraacetic acid (EDTA), in a 1:1 molar ratio, and polyethylenimine (PEI, 50 wt % in H_2O, Alfa Aesar, average M_n = 70,000). PEI is added until a pH value of 5−5.5 of the solution is obtained (approximately 1.3 g for 10 mL of solution final volume) to guarantee partial deprotonation of EDTA. Water is added to reach a final volume of 10 mL.

At this point, it was necessary to remove unbound ions and counterions from the solution: centrifugation up to constant volume of the retained fraction was performed with Amicon© ultracentrifugal units (10 kDa). Since the EDTA complexation of the metal ions is not complete, it was necessary to check the final concentration of metal ions in the retained fraction, which will differ from the initial nominal one. The final concentration of the metal ions was determined by inductively coupled plasma optical emission spectroscopy (ICP-OES) using a SPECTROFLAMEFMD-07 (Spectro Analytical Instruments Kleve, Germany) calibrated with standard solutions (Merck). Ultrapure water (18.2 MΩ cm resistivity) was used for progressive dilutions (Millipore laboratory equipment) to obtain the desired Ce^{4+} concentration. The same procedure was applied to prepare the solutions containing the dopant: $ZrO(NO_3)_2$ (Alfa Aesar 99.9%), $Gd(CH_3COO)_3$ (Sigma-Aldrich, 99.9%), and $La(NO_3)_3{\cdot}xH_2O$ (Sigma-Aldrich, 99.9%) were used as precursor salts.

The individual metal−polymer precursor solutions thus prepared were diluted or mixed according to the appropriate stoichiometry and molarity to prepare CeO_2 and doped CeO_2 precursor solutions. Different concentrations were evaluated. Due to the Y-stabilized ZrO_2 (YSZ) substrate low wettability, it was necessary to pretreat the substrates at 1000 °C, 4 h in air to ensure homogeneous deposition of the solution. The final polymeric solutions were spin coated on 7.5 × 7.5 mm^2 (100) YSZ crystalline substrates at 5000 rpm for 60 s. The samples were then crystallized at high temperatures in a Lenton tube furnace. Different growth conditions were employed; profiles A−E are reported in Figure 1. Profile A only consists of a 10 °C/min ramp up to the crystallization temperature and a dwell in static air atmosphere; in profiles B−E, a 30 min pyrolysis step at 600 °C was introduced, and different atmospheres (O_2, humid N_2), crystallization temperatures (1050 and 950 °C), and gas flows (0.94−2.82 L/min) were used. The specific conditions will be mentioned during the discussion.

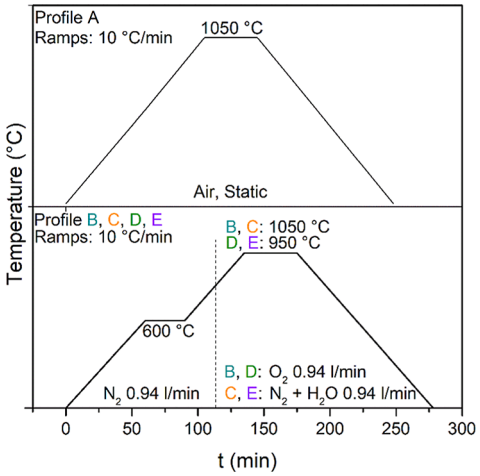

Figure 1. Schematic representation of the thermal treatments used for the deposition of CeO_2-based buffer layers.

Sample Characterization. The morphology of the buffer layers was characterized by atomic force microscopy (AFM) using the noncontact mode (Park Instruments XE 150), at room temperature and under an ambient atmosphere. AFM images were also used to perform a statistical analysis of the morphology of the samples. Roughness values and profile analysis parameters were evaluated with the AFM image processing software Gwyddion (http://gwyddion.net/) through the grain analysis tool.

The X-ray $\theta-2\theta$ and ω-scans were performed by using a Rigaku Geigerflex diffractometer working with Cu−Kα radiation. The (001) ω-scans were fitted using a pseudo-Voigt curve to extract the full width at half-maximum (fwhm) value. XRD ϕ-scans were performed by using a Smartlab Rigaku diffractometer equipped with a Eulerian cradle. The diffractometer was equipped with a primary monochromator, giving $CuK_{\alpha 1}$ radiation.

RESULTS AND DISCUSSION

Results. CeO_2 buffer layers with the PAD precursor solution were first grown with a 0.3 M precursor solution and thermal treatment labeled as A in Figure 1. The main features of this sample are summarized in Table 1. From the AFM images (Figure 2a), a morphology characterized by small grains and a value of roughness of R_{rms} = 3.4 nm is calculated for this sample. Moreover, the XRD diffractogram (Figure 2b) reveals the presence of both (111) and (002) orientations in the film, with a fwhm of the ω-scans as large as 5.8° revealing poor crystallinity (inset of Figure 2b). In order to try to obtain a smoother morphology, the solution concentration was decreased, and the thermal treatment was modified. The deposition of the 0.1 M solution with thermal treatment B leads to a more promising sample morphology (see Table 1). The CeO_2 sample treated with profile B is shown in Figure 2c: the film is very flat and uniform with large grains. The film thickness was estimated by measuring and averaging the depth of the largest, flat-bottomed holes that reveal a value of 22.4 nm. The line profile in Figure 2d is taken along the yellow

https://doi.org/10.1021/acs.cgd.5c00172
Cryst. Growth Des. 2025, 25, 3756−3766

Table 1. Summary of the Samples' Growth Conditions and Relevant Parameters[a]

sample	sol. conc (M)	treatment	gas flow (crystallization)	R_{rms} (nm)	area ($_{holes}$) (%)	hole depth (nm)	RX (*hkl*)
CeO_2	0.3	A	static	3.4	nd	nd	(111), (200)
CeO_2	0.1	B	0.94 L/min	8.4	22	19	(200)
evaluation of different dopant ions/concentrations							
CGO5 %	0.1	B	0.94 L/min	2.7	3	15	(200)
CLO5 %	0.1	B	0.94 L/min	15	5	25	(200)
CZO5 %	0.1	B	0.94 L/min	3.2	2.5	18	(200)
CZO10 %	0.1	B	0.94 L/min	9	22	24	(200)
evaluation of the oxygen flow during crystallization							
CZO5 %	0.1	B	0.94 L/min	3.2	2.5	18	(200)
CZO5 %	0.1	B	1.88 L/min	1.3	2	12	(200)
CZO5 %	0.1	B	2.82 L/min	2.4	6.4	15	(200)
evaluation of crystallization temperature/atmosphere							
CZO5 %	0.1	D	1.88 L/min	0.8	nd	nd	(200)
CZO5 %	0.1	C	1.88 L/min	2.8	2.2	20	(200)
CZO5 %	0.1	E	1.88 L/min	1.2	0.9	8	(200)
evaluation of film thickness							
CZO5 %	0.2	D	1.88 L/min	1.9	3	8	(200)
CZO5 %	0.2	E	1.88 L/min	3	1	10	(200)

[a]Acronyms and abbreviations-nd: not detected; R_{rms}: roughness (root-mean-square); CGO 5%: CeO_2 + 5% Gd^{3+}; CLO 5%: CeO_2 + 5% La^{3+}; CZO 5%: CeO_2 + 5% Zr^4.

dotted line in Figure 2c. The XRD measurement (Figure 2e) revealed the presence of only CeO_2 (200) reflections, and its excellent crystallinity is confirmed by an extremely narrow rocking curve (fwhm = 0.65°, Figure 2e, inset). Epitaxial growth is confirmed by the CeO_2 (111) ϕ-scan in Figure 2f, which reveals cube-on-cube growth of the film on the substrate. Excellent texture is confirmed by an average fwhm of the peaks of 1.11°. More details on this method can be found in the Supporting Information. However, the surface is characterized by large holes whose depth is approximately equivalent to the deposited film thickness (22% of the sample area consists of holes, whose average height is 19 nm, as reported in the label of Figure 2c; an example of the profile of the holes is shown in Figure 2e), which are responsible for the high roughness, R_{rms} = 8.4 nm. This exposure of the substrate is inconvenient for a buffer layer, which should give protection from unwanted diffusion of ions from the underlying layers. In order to understand the origin of this morphology, i.e., whether it forms during pyrolysis or crystallization, a series of quench experiments during profile B were carried out. In order to control the morphology of the films, it is important to determine if the hole formation is related to the evaporation/decomposition of the large polymer molecules during pyrolysis or to a different phenomenon occurring during crystallization. Therefore, samples were quenched (1) at the end of the pyrolysis plateau at 600 °C, (2) at the end of the ramp to crystallization temperature, and (3) in the middle of the crystallization plateau. The AFM images of the quenched samples are shown in Figure 3. In Figure 3a, sample 1 displays the expected featureless morphology of an amorphous pyrolyzed sample; samples 2 and 3 (Figure 3b,c), instead, show a progressive flattening of the surface with a simultaneous enlargement of the CeO_2 grains and exposed substrate (dewetted regions). These results show that surface flattening and hole formation occur simultaneously; therefore, a strategy to control these phenomena has to be employed, to obtain greater control on the surface morphology and suppress the exposure of the substrate. For reasons that will be discussed thoroughly in the next section, the strategy of doping, well-known from the literature[32,41] was attempted.

To evaluate the effect of different dopants on the morphology of the samples, doping was attempted with two aliovalent ions, La^{3+} and Gd^{3+}, and one isovalent ion Zr^{4+}, with a dopant concentration of 5%, a value that was proven successful for other chemical solution deposition techniques.[14,17,18,21,42] The three samples were all prepared by using thermal treatment B, and the resulting morphologies, analyzed via AFM, are shown in Figure 4a−c. The main features of these samples are summarized in Table 1. All three films are (100) oriented, with no sign of (111)-orientation: in Figure 4e, an example of the θ−2θ scan of the sample with 5% Zr is shown as a representative of the others. XRD data of the La- and Gd-doped CeO_2 can be found in the Supporting Information, Figures S4 and S5. The epitaxy of the film is unaffected by doping, as confirmed by the representative ϕ-scan in Figure 4f. Excellent texture is also confirmed in this case by an average fwhm of the peaks of 1.13°. For La^{3+} doping, the formation of large, flat grains is accompanied by a nonuniform development of the surface in the z direction, leading to very high surface roughness. Conversely, the use of Gd^{3+}, instead, leads to the formation of a much smoother surface in which few pinholes are visible, together with flat-topped grains. In addition, the presence of finer, rounded grains is visible on the surface. A longer dwell in the crystallization conditions causes the coalescence of these grains due to grain coarsening (see Figure S6). On the other hand, the Zr^{4+}-doped sample shows a much-improved morphology with respect to pure CeO_2, but also with respect to the Gd- and La-doped samples: the surface is flat and smooth, and very few pinholes are visible, whose depth does not reach the substrate. To evaluate the effect of dopant concentration, a sample with 10% Zr was prepared with thermal treatment B. The obtained morphology is similar to that of the La-doped sample, with large flat grains but also large and deep voids that increase the peak-to-valley distances, leading to a higher value of surface roughness (see Table 1). From these results, 5% Zr is selected as a doping agent for

https://doi.org/10.1021/acs.cgd.5c00172
Cryst. Growth Des. 2025, 25, 3756−3766

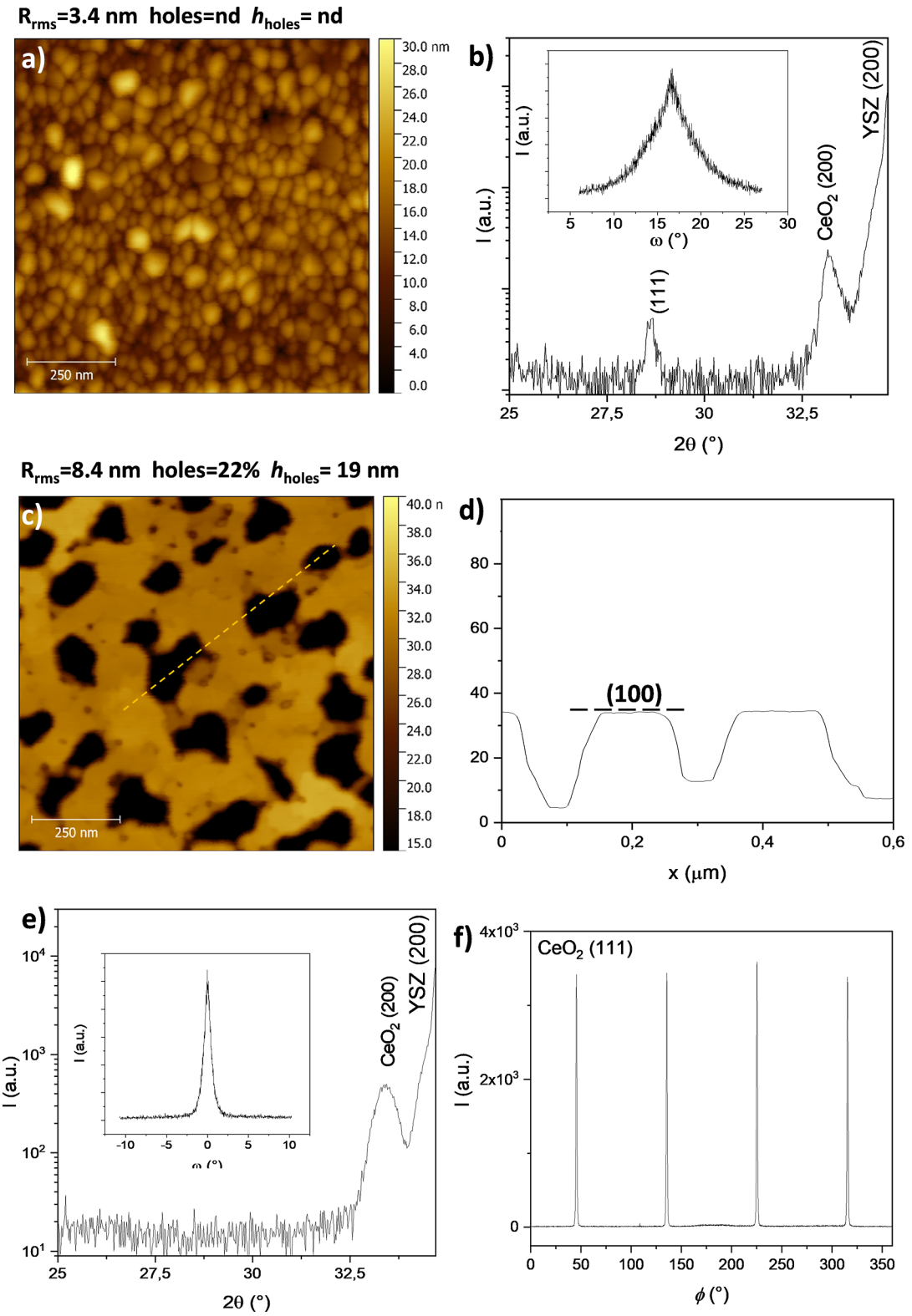

Figure 2. (a) AFM images of a CeO_2 layer obtained from a 0.3 M solution and thermal treatment A; (b) XRD θ–2θ scan of the sample with, in the inset, w scan of the CeO_2 (200) peak; (c) AFM image of a buffer obtained from a 0.1 M solution and thermal treatment B, (d) profile of the surface obtained from the AFM image along the yellow dotted line, (e) XRD θ–2θ scan of the sample with, in the inset, w scan of the CeO_2 (200) peak; and (f) XRD (111) ϕ-scan of the CeO_2 layer in (c–e) showing epitaxial growth of the film.

further optimization of the buffer layers, and only CeO_2–Zr5% (CZO) samples will be discussed in the following.

Another parameter that can be varied to optimize the sample morphology is the atmosphere during the thermal treatment. First of all, O_2 flow was varied: crystallization was carried out with a flow that is 2 and 3 times that of treatment B, and the relative results are summarized in Table 1 and presented in Figure 5a–c. If the O_2 flow during crystallization is doubled

https://doi.org/10.1021/acs.cgd.5c00172
Cryst. Growth Des. 2025, 25, 3756–3766

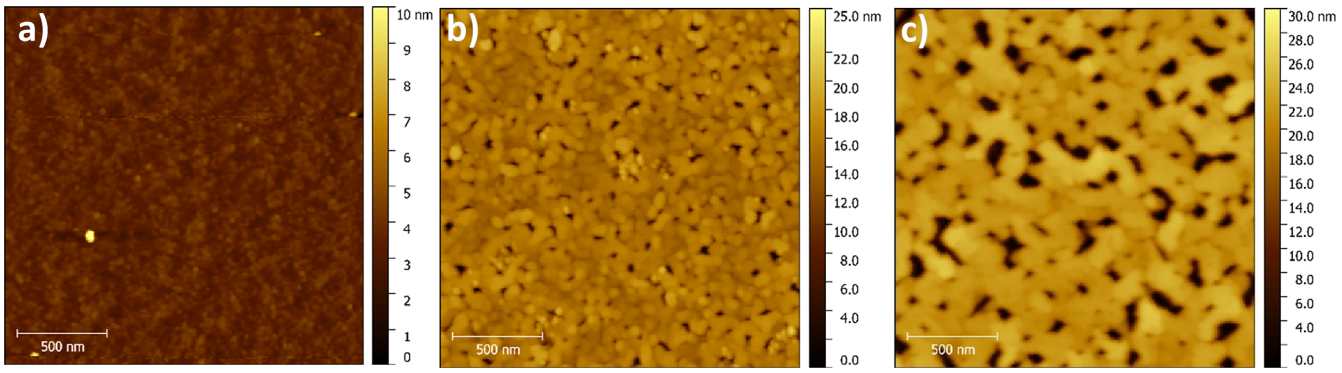

Figure 3. AFM images of CeO_2 samples quenched at different times of thermal treatment B. (a) Sample 1 quenched after pyrolysis at 600 °C for 30 min; (b) sample 2, quenched before crystallization at 1050 °C; and (c) sample 3, quenched during crystallization at 1050 °C.

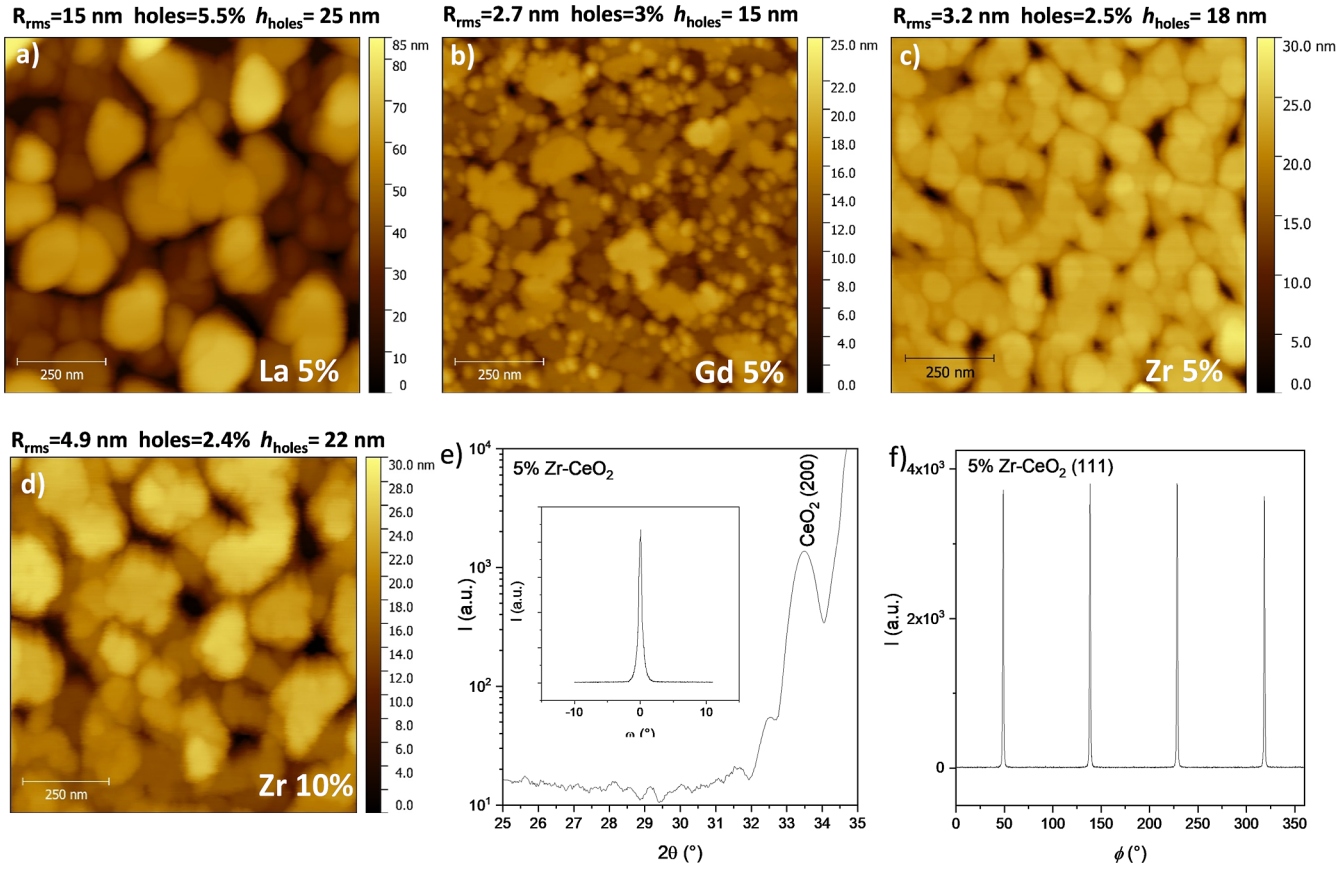

Figure 4. AFM images of the CeO_2 buffer layer with different kinds of doping ions obtained with thermal treatment B: (a) 5% La, (b) 5% Gd, (c) 5% Zr, and (d) 10% Zr. (e) XRD θ–2θ scan of the sample with 5% Zr, in the inset, ω-scan of the CeO_2 (200) peak, (f) XRD (111) ϕ-scan of a representative 5%-Zr CeO_2 buffer.

(Figure 5b) with respect to the standard value (Figure 5a), the surface is smoother, and with improved grain coalescence, limited faceting is observed, and fewer deep pinholes are formed. If an O_2 flow of 2.82 L/min is used (Figure 5c), that is, three times the standard value, the change in morphology becomes more visible, with a very smooth surface but also strong faceting in correspondence of the pinholes that now become wider and deeper. Proof of CZO faceting can be found if we draw a profile across one of the enlarged holes (Figure 5c yellow dotted line), which reveals the CeO_2 in which pyramids are truncated by large (100) planes. Relevant parameters of these samples are listed in Table 1. Since the main objective of this study is to optimize the morphology of a buffer layer, the optimal gas flow is 1.88 L/min since the resulting sample shows the lowest value hole percentage (2%) and of R_{rms} = 1.3 nm among the three conditions.

Once the optimal dopant ion and growth conditions are established, further control of the morphology was attempted by controlling the process of thermal grooving and surface reconstruction by crystallizing at lower temperatures. The first sample was prepared with the crystallization dwell at 950 °C (thermal profile D, Figure 1, relevant parameters in Table 1). The morphology of the obtained sample is shown in Figure 6a: in these conditions, we obtain a sample with low values of roughness (R_{rms} = 0.8 nm) that is also continuous, since the

https://doi.org/10.1021/acs.cgd.5c00172
Cryst. Growth Des. 2025, 25, 3756−3766

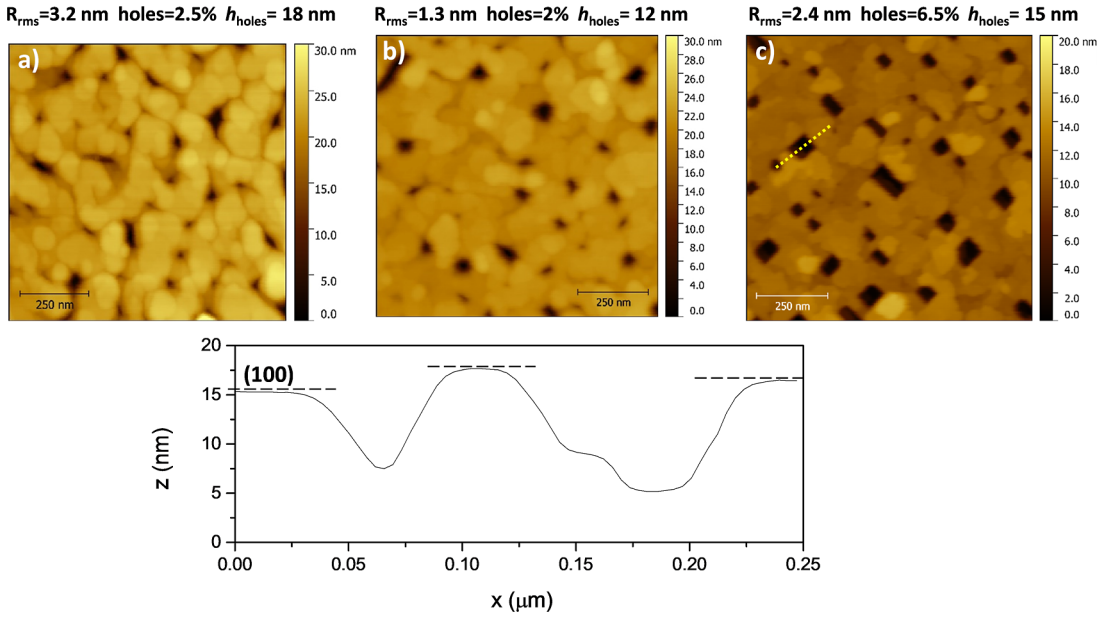

Figure 5. Upper panel: AFM images of three CZO samples crystallized with three different gas flows: (a) 0.94 L/min, (b) 1.88 L/min, and (c) 2.82 L/min. Lower panel: profile extracted along the yellow dotted line in the AFM image of Figure 4, right.

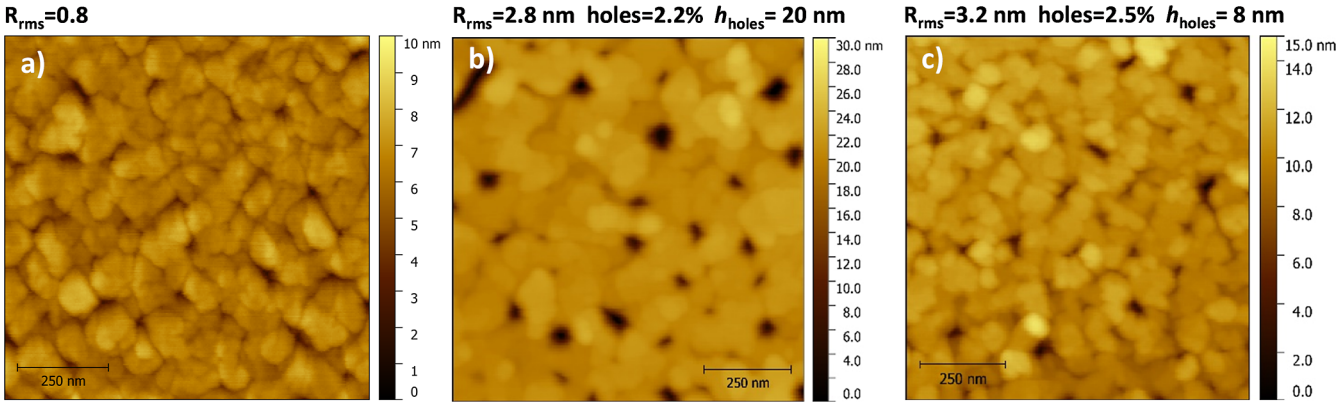

Figure 6. AFM images of CZO 5% samples crystallized in different conditions: (a) profile D, 950 °C, O_2, (b) profile C, 1050 °C N_2/H_2O, (c) profile E, 950 °C N_2/H_2O.

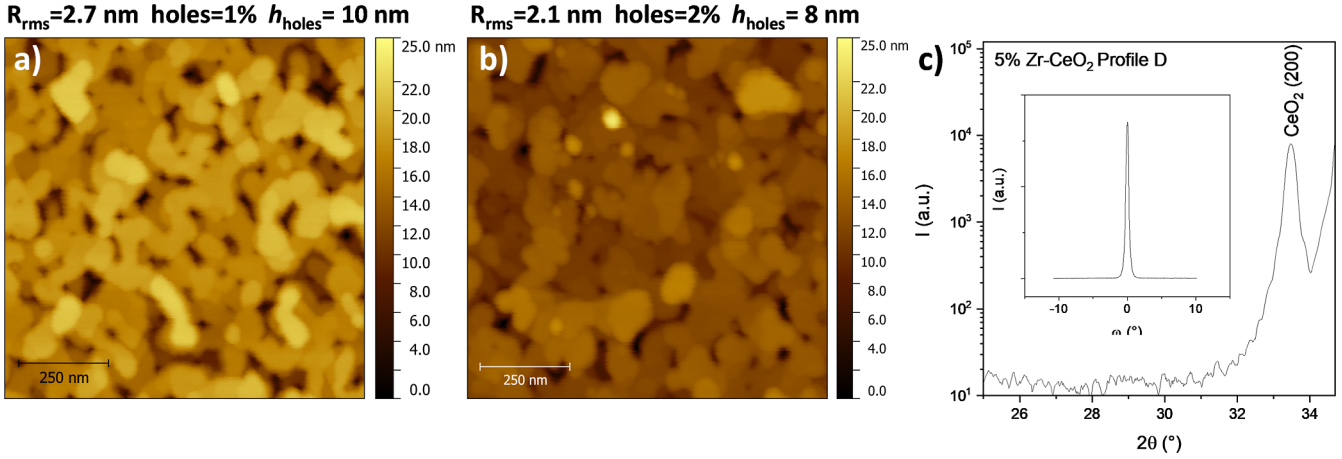

Figure 7. AFM images of two CZO 5% samples from a 0.2 solution: (a) prepared with profile D; (b) prepared with profile E; and (c) XRD data of the sample in (a), as a representative for both.

depth of the small visible pinholes does not reach 4 nm, which is less than the film thickness.

The growth of epitaxial CZO buffer layers was also attempted in less oxidizing conditions: in particular, a

https://doi.org/10.1021/acs.cgd.5c00172
Cryst. Growth Des. 2025, 25, 3756−3766

crystallization treatment in humid N_2 as proposed in the work by Solovyov et al.[43] Samples were prepared with two different crystallization temperatures: one sample with treatment C and the other sample with treatment E; the AFM images of the samples are presented in Figure 6b,c, and the main features are summarized in Table 1. The former sample (treated with profile C) shows a terraced surface with flat grains but holes approximately 20 nm deep that extend down to the substrate (Figure 6b). The sample crystallized at 950 °C (treatment E), instead, shows a fine smooth surface with a much lower peak-to-valley ratio, reduced R_{rms}, and few shallow nanopores (Figure 6c, Table 1).

Two more films were prepared to evaluate the effect of the film thickness on thermal grooving. With chemical deposition methods, the final film thickness can be easily controlled by acting on the precursor solution concentration. Therefore, two samples were prepared from a 0.2 M solution, a concentration that is twice the standard 0.1 M discussed until now. With such a concentration, the film thickness is estimated around 33 nm, with the same procedure used for CeO_2 films. One film was treated with profile D and the other with profile E. The AFM images of such samples are shown in Figure 7a,b, see Table 1 for relevant features. From XRD analysis, both films are crystalline and (001) oriented (Figure 7c). In both cases, we observe large flat grains, but in the sample crystallized in an oxygen atmosphere (Figure 7a), the excursion in the z direction is higher than in the sample crystallized in humid N_2 (Figure 7b). This causes a slight increase in roughness in the sample prepared in oxygen. In both cases, the number of holes is very low and, most importantly, their depth is not sufficient to reach the substrate. More in detail, holes 8−10 nm deep are still visible, but in a sample ∼35 nm thick, they do not reach the substrate.

DISCUSSION

The development of a CeO_2-based buffer layer is a widely studied topic, together with the detailed characterization of its structure, different surface energies, surface reconstruction, and stabilization mechanisms. In this paper, a systematic study of polymer-assisted-deposition of (l00)-oriented, epitaxial CeO_2-based films is proposed, with the aim of optimizing the methodology so as to obtain the characteristic required from a buffer layer: complete coverage of the substrate (no holes), low roughness values, and high percentage of an atomically flat surface area. According to our results, these conditions are met when samples are prepared with profile E.

Cerium oxide is a compound with a high melting temperature (2500 °C), with very limited mobility of Ce atoms at practical deposition temperatures (around 1000 °C). According to Thornton's classification scheme, CeO_2 films can be described as Zone-2 films, which would be dense arrays of columnar grains with faceted surfaces and voided grain boundaries.[43,44] Stoichiometric CeO_2 crystallizes in the face-centered cubic fluorite-type structure with a lattice parameter of 5.41 Å. The substrate employed in this work, yttria-stabilized zirconia (YSZ), crystallizes in the same structure with a lattice parameter of 5.13 Å. Despite the relatively large lattice mismatch of around 5%, ceria thin films were reported to grow epitaxially on (100) YSZ.[32,33,41,45] In a first approximation, the CeO_2 film growth mode can be predicted from the evaluation of the wetting conditions derived from Young's equation: the change in surface energy $\Delta\gamma$ can be expressed as $\Delta\gamma = \gamma_f + \gamma_i - \gamma_s$, where γ_f, γ_i, and γ_s are the surface energies of the film, the film/substrate interface, and the substrate, respectively. In this case, γ_f and γ_s correspond to the energy of the (001) surface since it is both the orientation of YSZ and the film orientation. The interface energies can be considered negligible with respect to γ_s, since, despite the lattice mismatch, the CeO_2 film does grow epitaxially on YSZ that has the same crystallographic structure.[46−48] Therefore, since $\gamma_{CeO2} = 3.25$ J m^{-2}[48] and $\gamma_{YSZ} = 1.75$ J m^{-2}[49] and γ_i can be neglected with respect to the other terms, $\gamma_f + \gamma_i > \gamma_s$ and the system will grow following a 3D or Volmer−Weber growth mode, with the formation of islands that will enlarge and coalesce into a continuous film[46,50,51] that in our system grows epitaxially with a cube-on-cube relationship with the substrate. However, it is known from the literature that the CeO_2 (001) surface energy is approximately two times higher than the other low-index faces, (111) and (110), due to a high polar character; therefore, the exposure of (001) is energetically disfavored with respect to the other two, i.e., in CeO_2, the formation energy of the island edge sides is negative when the edge-side facet is (111) and the top facet is (001).[48,52,53] This leads to the phenomenon of faceting so as to maximize exposure of the more energetically stable facets such as (110), (111), or other low energy surfaces.[40,54,55] The microstructural instability in thin films, and the consequential surface modification during crystallization, is a well-known phenomenon carefully discussed in Seifert et al.,[56] and it does depend not only on the relative surface energy values but also on the film thickness. In our thin film regime (<100 nm), it was shown that surface pits can spontaneously form and grow further up to the point of uncovering the substrate. It follows that the preparation of an epitaxial buffer layer with the (001) specific orientation is not trivial, and strategies to control the morphology of the obtained surface need to be applied.

In principle, high-temperature annealing should provide the half-a-monolayer of oxygen required to annul the surface dipole moment, i.e., surface reconstruction in oxidizing conditions can control surface polarity.[53,57] Therefore, the most basic thermal profile (profile A, Figure 1) was applied as the first option. The resulting film, however, was not satisfactory due to the presence of (111)-oriented grains. The rough morphology of the sample is thought to be caused by the precursor solution decomposition mechanism that affects the microstructure of the film during the pyrolysis of the organic components. From the literature, it is known that the CeO_2 PAD precursor solution is subject to an exothermic decomposition around 500 °C when treated in oxygen, which causes violent gas evolution through the bulk of the film and severe increase of the film porosity. On the other hand, when heated under an inert atmosphere, the mass loss is less abrupt, and the involved reactions are far less exothermic with respect to the previous case.[32,33] For this reason, a pyrolysis step in an inert atmosphere was added (Figure 1, profile B). With this treatment, the epitaxial film morphology is completely different, with a smooth surface and large voids reaching the substrate. The exposure of the sides of the truncated pyramids during crystallization causes a significant increase in the film roughness due to the large peak-to-valley distances, as can be seen from the AFM profiles of the CeO_2 sample shown in Figure 2c. To ascertain that this morphology is the result of the grain growth and surface reconstruction during crystallization and not of other unpredicted dewetting phenomena occurring before, quench experiments were performed. From the AFM images of Figure 3, we can see how the film evolves during the

https://doi.org/10.1021/acs.cgd.5c00172
Cryst. Growth Des. 2025, 25, 3756−3766

ramp up to the crystallization temperature and during the subsequent dwell, reconstructing, and exposing the substrate. From this experiment, we can conclude that the exposition of the substrate is not due to a violent decomposition reaction with a large amount of gas release, but it occurs at higher temperatures, where the crystallization and surface reconstruction/thermal grooving processes overlap. We also infer that the oxygen provided during the thermal treatment can indeed provide some stabilization of the (001) surface, but not enough to limit the preferential exposure of the other faces with a consequential increase of surface roughness.

To further control the morphology of the samples, another approach to stabilize the (001) facet through doping is attempted. It is known from the literature that doping can have a beneficial effect in this sense, since it influences the surface oxygen content by introducing compensating charges on the outer planes that can reduce the (001) polarity.[52,53] In principle, stabilization of the surface is obtained because of the formation of oxygen vacancies caused by the introduction of an aliovalent ion M^{3+}. Ions of smaller ionic size and lower oxidation state substitute the Ce^{4+} ions in the fluorite lattice, and then the oxygen vacancies are created and the bound electrons get delocalized. These delocalized electrons may either get trapped into vacancies or contribute to the conduction current. Thus, formation of oxygen vacancies leads to the reduction of the valence state of a small amount of the Ce ions in the host lattice. However, not only the electronic modifications but also structural rearrangements caused by the difference in size between the dopant and Ce should be considered, which is why also isovalent ions M^{4+} were used for doping, with the aim of studying how the effect of an increased/reduced ionic radius influences the surface stability. It was calculated that introducing ions with smaller radius than Ce makes the formation of oxygen vacancies a spontaneous process.[58] In particular, the smaller size of M^{4+} causes different coordination inside the lattice and the formation of weak M-O bonds. Therefore, even if M^{4+} does not introduce electronic imbalances, an effect on the morphology of the film can be expected.[41,59−62] Thus, CeO_2 films were prepared with La^{3+}, Gd^{3+}, and Zr^{4+} doping. It should also be pointed out that another issue related to CeO_2 thin film processing is the reduced mobility of the ions, which represents the main consequence of preparing films at temperatures so far from the melting point of the material (undercooling conditions).[63,64] During crystallization, lateral grain size increases, leading to the formation of flat grains and to a significant smoothing of the surface, but this phenomenon is counterbalanced by thermal grooving, which inhibits lateral grain growth when the grain size reaches a value of approximately twice the film thickness.[50,51] Since the formation of large grains and low values of roughness are necessary for optimal buffer layers, this tendency should be controlled and grain size maximized. Again, doping can have a beneficial effect also in this case: it was shown that lateral grain size is closely related (also) to the grain boundary mobility and that grain boundary motion is linked to the presence of oxygen vacancies, whose role is to facilitate diffusion across the grain boundary and the evolution of the microstructure during recrystallization.[41,62]

For comparison, the samples with 5% doping of La^{3+}, Gd^{3+}, and Zr^{4+} are presented in Figure 4a−c. With lanthanum (Figure 4a), thanks to the increased grain boundary mobility, the grain size as well as its height is significantly increased, leaving an epitaxial film with a very high R_{rms} due to a large peak-to-valley distance, which is not optimal for the purpose of a buffer layer. This situation is further enhanced if the sample is subject to a longer crystallization process, with a visible coarsening that leaves even larger regions of the substrate exposed (Supporting Information). With gadolinium (Figure 4b), the amount of the terraced surface is not only increased, but also the formation of a non-negligible number of pinholes is observed as in.[41] Again, the use of a longer crystallization treatment helps to complete the coarsening process, with the disappearance of the smaller-sized grains and the enlargement of the bigger ones, but also in this case, the obtained morphology is not ideal for a buffer layer because of the high number of visible pores on the surface. The sample with zirconium, instead, shows a flat and uniform surface (Figure 4c), with low values of roughness and increased coverage of the substrate. This difference in behavior can be traced back to the valence of the dopant ions: indeed, more oxygen vacancies and therefore more surface reactivities are obtained with doping with aliovalent ions, with respect to isovalent ions, that only cause lattice distortion and weaken the M−O bonds. Higher reactivity and grain boundary mobility cause abnormal grain growth for La-doped and Gd-doped CeO_2, but this does not happen with Zr-doped CeO_2. The situation changes if a sample with 10% Zr is prepared under the same conditions as the 5% sample. As shown in Figure 4d, the higher amount of doping increases surface roughness, leaving a morphology similar to that of the La-doped sample.

Despite the significant improvement of the surface morphology of Zr-doped CeO_2, the presence of small pinholes as deep as 20 nm makes further optimization of the process necessary to obtain a continuous layer. To ascertain that the almost-full coverage of the substrate is not caused by the reduced crystallization time, the duration of the dwell was increased up to 8 h (see Figure S7 in the Supporting Information). No relevant difference can be observed to arise from such a longer treatment, which leads to the conclusion that pinholes are caused by energy-minimization-induced processes that quickly reach equilibrium.

It is known that the morphology of the sample is due to two separate contributions: the oxygen surface content, which is determined by charge neutrality, and the cerium lattice ordering, which originates during annealing, where grain growth and surface reconstruction occur simultaneously.[43] Since oxygen content was proven to be a key parameter for the stabilization of the desired (001) surface,[53] samples were prepared with different oxygen flows at atmospheric pressure. In Figure 5a−c, the effect of the increase in oxygen on the Zr-doped CeO_2 film surface is shown. We observe that two phenomena are occurring simultaneously, the flattening of the topmost (001) surface of the grains and the enlargement of the pores with exposure of the sides of the grains: higher flows promote surface reconstruction, probably increasing the kinetics of the process by renewing more quickly the atmosphere at the reactive surface. It follows that the right oxygen flow must be chosen so as to balance the two processes and to maximize (001) and minimize other surfaces exposure. In this case, the intermediate value of gas flow leads to the best combination of R_{rms} and pore size/density.

To control the thermal grooving/surface reconstruction processes occurring during crystallization, another strategy is to lower the crystallization temperature. Indeed, these phenomena occur through a self-diffusion process, and it is

https://doi.org/10.1021/acs.cgd.5c00172
Cryst. Growth Des. 2025, 25, 3756−3766

exponentially dependent on temperature according to an Arrhenius-like relationship for the diffusion coefficient $D = D_0 \exp\left(\frac{-Q_d}{K_b T}\right)$, where D_0 is a pre-exponential factor that depends on parameters such as the lattice constant and other geometrical data, Q_d is the activation energy for diffusion, and k_B is the Boltzmann constant.[46,47] In this case, attention should be paid since high temperatures are necessary for epitaxial growth: minimization of hole formation cannot be favored at the expense of epitaxy. For this purpose, profile D was developed, in which the crystallization temperature was reduced from 1050 to 950 °C.

The clear effect of temperature reduction is visible in the AFM image of the sample (Figure 6a). In this case, the morphology is characterized by flat-topped grains and a no visible hole, leaving a value of roughness <1 nm. This effect is supposed to be due to a reduced kinetic of surface reconstruction and groove formation, which is responsible for the not complete deepening of the grooves at grain boundary that therefore do not reach the interface with the substrate.

Since one of the most widespread applications of CeO_2 buffer layers is in the coated conductor technology, the growth of the buffers must be optimized also in conditions that are compatible with the substrates commonly employed in this case, e.g., biaxially textured, flexible metallic tapes. The main drawback of the developed methodology is that it requires oxidizing conditions that cannot be applied to metallic substrates without causing their degradation. This is why the crystallization atmosphere was changed from pure oxygen to humid N_2 (profile E). This atmosphere was selected because it is known that water can provide the hydroxylation required to favor the exposure of the (001).[65] Samples were prepared with profiles C and E to evaluate both the effect of the atmosphere and the crystallization temperatures. Results shown in Figure 6b,c demonstrate how water is as efficient as oxygen in the promotion of a flat morphology and that working at slightly lower temperatures can effectively reduce the number of pinholes present on the surface and their size. With profile E, a morphology suitable for a buffer layer is obtained, using conditions that are more friendly toward metallic substrates.

On the other hand, temperature is not the only parameter that can be tuned to control hole formation. Several models were developed to describe the formation of grooves during thermal annealing of films, but even if the formal treatment slightly differs between them, the basic principles governing the phenomenon are the same. Hole formation starts at grain boundaries and grain boundary triple junctions, and it was demonstrated that the number of holes that forms during thermal annealing inversely scales with the film thickness, which is an easy parameter to control with chemical deposition techniques.[66] Therefore, a further step was taken in the optimization of the buffer surface by doubling the precursor concentration. Two samples were prepared with a precursor solution with a doubled concentration (0.2 M) following profiles D and E. The effect of higher thicknesses on the films' morphology is, in this case, that of preventing the grooves from reaching the substrate surface, thus leading to the formation of a continuous film. Indeed, in our samples, the density of the grooves decreases, and their depth is reduced. This is in contrast with what happens in thinner films, where the holes clearly reach the substrate.

In conclusion, this work shows how the morphology of solution-derived CeO_2 thin films can be successfully controlled so as to induce and promote the features most relevant to a buffer layer, e.g., large flat grains, continuity, and low values of surface roughness. It should be stressed that, in accordance with the theory of thermal grooving[39,67] and previously publisher results,[39] the residual faceting visible on the surface does not compromise the buffer continuity. By understanding the parameters involved in the determination of the sample morphology, the thermodynamic processes behind surface reconstruction, and the possible strategies able to counterbalance them, it is possible to tune the properties of final samples according to specific needs. Moreover, these results can be applied not only to the PAD method but also to other popular chemical solution deposition methods such as MOD or sol−gel, since the crystallization process is independent of the type of precursors used.

■ ASSOCIATED CONTENT

Supporting Information

Supporting Information is available The Supporting Information is available free of charge at https://pubs.acs.org/doi/10.1021/acs.cgd.5c00172.

Detailed description of the procedure for thickness evaluation with AFM images, X-ray diffractogram of the 5% Gd-CeO_2 buffer, X-ray diffractogram of the 5% La−CeO_2 buffer, AFM image of a 5% Gd-CeO_2 sample treated with a 2 h and 30 min dwell at 1050 °C, and AFM image of a 5% Zr−CeO_2 sample treated with an 8 h dwell at 1050 °C (PDF)

■ AUTHOR INFORMATION

Corresponding Author

L. Piperno − *ENEA Frascati Research Centre, Superconductivity Laboratory, Frascati 00044, Italy;* orcid.org/0000-0002-2775-8087; Email: laura.piperno@enea.it

Authors

A. Vannozzi − *ENEA Frascati Research Centre, Superconductivity Laboratory, Frascati 00044, Italy;* orcid.org/0000-0003-4628-4312

A. Mancini − *ENEA Frascati Research Centre, Superconductivity Laboratory, Frascati 00044, Italy*

R. B. Sonher − *Centre for Superconductivity, Spintronics and Surface Science, Technical University of Cluj-Napoca, Cluj-Napoca 400114, Romania*

G. Sotgiu − *Department of Industrial, Electronic, and Mechanical Engineering, Roma Tre University, Rome 00146, Italy*

G. Celentano − *ENEA Frascati Research Centre, Superconductivity Laboratory, Frascati 00044, Italy*

Complete contact information is available at: https://pubs.acs.org/10.1021/acs.cgd.5c00172

Author Contributions

The manuscript was written through contributions of all authors. All authors have given approval to the final version of the manuscript.

Notes

The authors declare no competing financial interest.

https://doi.org/10.1021/acs.cgd.5c00172
Cryst. Growth Des. 2025, 25, 3756−3766

REFERENCES

(1) Trovarelli, A. Catalytic Properties of Ceria and CeO2-Containing Materials. *Catal. Rev.* **1996**, *38* (4), 439−520.

(2) Schwab, R. G.; Steiner, R. A.; Mages, G.; Beie, H. J. Properties of CeO2 and CeO2−x Films Part II. High Temperature Properties. *Thin Solid Films* **1992**, *207* (1−2), 288−293.

(3) Wang, Y.; Wang, H.; Li, C. S.; Feng, J. Q.; Jin, L. H.; Yu, Z. M.; Odier, P.; Zhang, P. X. Effective Removal Procedure of Residual Carbon in CeO2-x Films Fabricated via MOD Method. *Ceram. Int.* **2015**, *41* (10), 14270−14275.

(4) Stanek, C. R.; Tan, A. H. H.; Owens, S. L.; Grimes, R. W. Atomistic Simulation of CeO2 Surface Hydroxylation: Implications for Glass Polishing. *J. Mater. Sci.* **2008**, *43* (12), 4157−4162.

(5) Tuller, H. L.; Nowick, A. S. Defect Structure and Electrical Properties of Nonstoichiometric CeO2 Single Crystals. *J. Electrochem. Soc.* **1979**, *126* (2), 209−217.

(6) Beie, H. J.; Gnörich, A. Oxygen Gas Sensors Based on CeO2 Thick and Thin Films. *Sens Actuators B Chem.* **1991**, *4* (3−4), 393−399.

(7) Jacobsen, S. N.; Madsen, L. D.; Helmersson, U. Epitaxial Cerium Oxide Buffer Layers and YBa 2 Cu 3 O 7−δ Thin Films for Microwave Device Applications. *J. Mater. Res.* **1999**, *14* (6), 2385−2393.

(8) Tian, D.; Lin, B.; Yang, Y.; Chen, Y.; Lu, X.; Wang, Z.; Liu, W.; Traversa, E. Enhanced Performance of Symmetrical Solid Oxide Fuel Cells Using a Doped Ceria Buffer Layer. *Electrochim. Acta* **2016**, *208*, 318−324.

(9) Piperno, L.; Vannozzi, A.; Sotgiu, G.; Celentano, G. CeO2-Based Buffer Layers via Chemical Solution Deposition: Critical Issues and Latest Developments. *J. Eur. Ceram. Soc.* **2021**, *41*, 2193−2206.

(10) Fukano, T.; Nozaki, H.; Funayama, K.; Katsuno, T.; Koganezawa, T.; Harada, M.; Kawaura, H. Depth Profiles of Crystallinity and Preferential Orientation and Surface Characteristics of Sputter-Deposited CeO_2 Thin Film Buffer Layers on Sapphire Substrates Evaluated Through Two-Dimensional Grazing-Incidence X-Ray Diffraction. *Surf. Interface Anal.*; Wiley Online Library, 2025; Vol. *57*, pp 121−130..

(11) Holzapfel, B.; Wiesmann, J. Substrates and Functional Buffer Layers. *Handbook of Superconductivity* **2022**, 334−347.

(12) Jung, S. Y.; Choi, H. J.; Lee, J. Y.; Kim, M. S.; Ning, R.; Han, D. H.; Kim, S. K.; Won, S. O.; Lee, J. H.; Jang, J. S.; Jang, H. W.; Baek, S. H. Evolution of Microcracks in Epitaxial CeO2 Thin Films on YSZ-Buffered Si. *Electron. Mater. Lett.* **2024**, *20* (4), 484−490.

(13) Coll, M.; Gázquez, J.; Hühne, R.; Holzapfel, B.; Morilla, Y.; García-López, J.; Pomar, A.; Sandiumenge, F.; Puig, T.; Obradors, X. All Chemical YBa2Cu307 Superconducting Multilayers: Critical Role of CeO2 Cap Layer Flatness. *J. Mater. Res.* **2009**, *24* (4), 1446−1455.

(14) Vannozzi, A.; Mancini, A.; Rizzo, F.; Petrisor, T.; Augieri, A.; Celentano, G.; Rufoloni, A.; Rubanov, S.; Pinto, V.; Fabbri, F.; Angrisani Armenio, A.; Galluzzi, V. Growth of Biaxially-Textured La2Zr2O7 and Zr-Doped CeO2 on Cold-Rolled Ni-W Substrate by CSD. *IEEE Trans. Appl. Supercond.* **2018**, *28* (4), 1−5.

(15) Hu, X.; Zhong, Y.; Zhong, H.; Fan, F.; Sang, L.; Li, M.; Fang, Q.; Zheng, J.; Song, H.; Lu, Y.; Liu, Z.; Bai, C.; Guo, Y.; Cai, C. Effect of Template Post-Annealing on Y(Dy)BaCuO Nucleation on CeO2 Buffered Metallic Tapes. *Phys. C (Amsterdam, Neth.)* **2017**, *539*, 13−18.

(16) Vannozzi, A.; Prili, S.; Sylva, G.; Masi, A.; Armenio, A. A.; Mancini, A.; Pinto, V.; Rufoloni, A.; Piperno, L.; Augieri, A.; Rizzo, F.; Manfrinetti, P.; Braccini, V.; Putti, M.; Silva, E.; Celentano, G. Epitaxial Zr-Doped CeO2films by Chemical Solution Deposition as Buffer Layers for Fe(Se,Te) Film Growth. *Supercond. Sci. Technol.* **2020**, *33* (8), 084004.

(17) Vannozzi, A.; Piperno, L.; Rufoloni, A.; Botti, S.; Bonfigli, F.; Iebole, M.; Savio, L.; Cialone, M.; Masi, A.; Mancini, A.; Augieri, A.; Celentano, G.; Putti, M.; Putti, M.; Braccini, V.; Rufoloni, A.; Botti, S.; Bonfigli, F.; Masi, A.; Mancini, A.; Celentano, G.; Savio, L.; Cialone, M.; Putti, M. Zr:CeO2 Buffer by CSD on Ni-W Substrate for low-Cost Fe(Se,Te) Coated Conductor. *IEEE Trans. Appl. Supercond.* **2024**, *34*, 1−5.

(18) Piperno, L.; Vannozzi, A.; Augieri, A.; Masi, A.; Mancini, A.; Rufoloni, A.; Celentano, G.; Braccini, V.; Cialone, M.; Iebole, M.; Manca, N.; Martinelli, A.; Meinero, M.; Putti, M.; Meledin, A. High-Performance Fe(Se,Te) Films on Chemical CeO2-Based Buffer Layers. *Sci. Rep.* **2023**, *13* (1), 1−11.

(19) Piperno, L.; Vannozzi, A.; Pinto, V.; Augieri, A.; Armenio, A. A.; Rizzo, F.; Mancini, A.; Rufoloni, A.; Celentano, G.; Braccini, V.; Cialone, M.; Iebole, M.; Manca, N.; Martinelli, A.; Putti, M.; Sotgiu, G.; Meledin, A. Chemical CeO2-Based Buffer Layers for Fe(Se,Te) Films. *IEEE Trans. Appl. Supercond.* **2022**, *32* (4), 1−5.

(20) Piperno, L.; Vannozzi, A.; Rizzo, F.; Masi, A.; Rufoloni, A.; Celentano, G.; Braccini, V.; Cialone, M.; Iebole, M.; Martinelli, A.; Savio, L.; Putti, M.; Meledin, A.; Sotgiu, G. Low-Cost Architecture for Iron-Based Coated Conductors. *iScience* **2024**, *27* (10), 111032.

(21) Augieri, A.; Mancini, M. R.; Vannozzi, A.; Angrisani, A. A.; Fabbri, F.; Rizzo, F.; Mancini, A.; Rufoloni, A.; Galluzzi, V.; Celentano, G.; Sotgiu, G. MOD oxide buffer layers on metallic substrates for YBCO coated conductors; *MRS Online Proceedings Library*, **2013**; Vol. *1579*..

(22) Augieri, A.; Vannozzi, A.; Mancini, R.; Angrisani, A. A.; Fabbri, F.; Galluzzi, V.; Rufoloni, A.; Rizzo, F.; Mancini, A.; Celentano, G.; Colantoni, I.; Davoli, I.; Pompeo, N.; Sotgiu, G.; Silva, E. MOD Derived Pyrochlore Films as Buffer Layer for All-Chemical YBCO Coated Conductors. *IEEE Trans. Appl. Supercond.* **2013**, *23* (3), 6600505.

(23) Bian, W.; Chen, Y.; Tang, X.; Zhang, W.; Zhao, G.; Wang, Z. Sol−Gel Deposition of High-Performance Re0.2Ce0.8O2/La2Zr2O7 Composite Buffer Layers on Ni−W Tapes for YBCO Coated Conductors. *J. Solgel Sci. Technol.* **2016**, *77* (1), 94−99.

(24) Obradors, X.; Puig, T. Coated Conductors for Power Applications: Materials Challenges. *Supercond. Sci. Technol.* **2014**, *27* (4), 044003.

(25) MacManus-Driscoll, J. L.; Wimbush, S. C. Processing and Application of High-Temperature Superconducting Coated Conductors. *Nat. Rev. Mater.* **2021**, *6*, 587−604.

(26) Obradors, X.; Puig, T.; Pomar, A.; Sandiumenge, F.; Pinol, S.; Mestres, N.; Castano, O.; Coll, M.; Cavallaro, A.; Palau, A.; et al. Chemical Solution Deposition: A Path towards Low Cost Coated Conductors. *Supercond. Sci. Technol.* **2004**, *17* (8), 1055−1064.

(27) Vanpoucke, D.; Cottenier, S.; Van Speybroeck, V.; Bultinck, P.; Van Driessche, I.; Speybroeck, V. Van.; Bultinck, P.; Driessche, I. Van. Tuning of CeO 2 Buffer Layers for Coated Superconductors through Doping. *Appl. Surf. Sci.* **2012**, *260*, 32−35.

(28) Vlad, V. R. *Growth and Characterization of Chemical Solution Based Nanostructured Coated Conductors with CeO2 Cap Layers*; Universitat Autònoma de Barcelona, 2011.

(29) McCleskey, T. M.; Burrell, A. K.; Jia, Q.; Lin, Y. *Polymer-Assisted Deposition of Films* **2008**, *7*, 365.

(30) Jia, Q. X.; McCleskey, T. M.; Burrell, A. K.; Lin, Y.; Collis, G. E.; Wang, H.; Li, A. D. Q.; Foltyn, S. R. Polymer-Assisted Deposition of Metal-Oxide Films. *Nat. Mater.* **2004**, *3* (8), 529.

(31) Zou, G. F.; Zhao, J.; Luo, H. M.; McCleskey, T. M.; Burrell, A. K.; Jia, Q. X. Polymer-Assisted-Deposition: A Chemical Solution Route for a Wide Range of Materials. *Chem. Soc. Rev.* **2013**, *42* (2), 439−449.

(32) Mos, R. B.; Petrisor, T.; Nasui, M.; Calleja, A.; Puig, T.; Ciontea, L.; Petrisor, T. Enhanced Structural and Morphological Properties of Gd-Doped CeO 2 Thin Films Obtained by Polymer-Assisted Deposition. *Mater. Lett.* **2014**, *124*, 306−309.

(33) Calleja, A.; Mos, R. B.; Roura, P.; Farjas, J.; Arbiol, J.; Ciontea, L.; Obradors, X.; Puig, T. Growth of Epitaxial CeO2 Buffer Layers by Polymer Assisted Deposition. *Mater. Res. Soc. Symp. Proc.* **2012**, *1449*, 31.

(34) Mos, R. B.; Petrisor Jr, T.; Nasui, M.; Mesaros, A.; Gabor, M. S.; Senila, M.; Ware, E.; Ciontea, L.; Petrisor, T. Epitaxial La0. 7Sr0. 3MnO3 Nanostructures Obtained by Polymer-Assisted Surface Decoration (PASD). *Mater. Lett.* **2016**, *171*, 281−284.

https://doi.org/10.1021/acs.cgd.5c00172
Cryst. Growth Des. 2025, 25, 3756−3766

(35) Piperno, L.; Armenio, A. A.; Vannozzi, A.; Mancini, A.; Rizzo, F.; Augieri, A.; Pinto, V.; Rufoloni, A.; Mos, R. B.; Ciontea, L. Polymer-Assisted Surface Decoration for Critical Current Enhancement in \ch{YBa2Cu3O$_{7-X}$}- x Films. *Appl. Surf. Sci.* **2019**, *484*, 237−244.
(36) Piperno, L.; Angrisani Armenio, A.; Vannozzi, A.; Mancini, A.; Rizzo, F.; Augieri, A.; Pinto, V.; Rufoloni, A.; Mos, R. B.; Ciontea, L.; Petrisor, T.; Petrisor, T.; Sotgiu, G.; et al. Polymer-Assisted Surface Decoration for Critical Current Enhancement in YBa 2 Cu 3 O 7−x Films. *Appl. Surf. Sci.* **2019**, *484*, 237−244.
(37) Armenio, A. A.; Piperno, L.; Petrisor, T.; Vannozzi, A.; Pinto, V.; Rizzo, F.; Augieri, A.; Mancini, A.; Rufoloni, A.; Mos, R. B.; Ciontea, L.; Petrisor, T.; Sotgiu, G.; et al. Nanostructured Templates for Critical Current Density Enhancement in YBa2Cu3O7−x Films. *Supercond. Sci. Technol.* **2020**, *33* (9), 094003.
(38) Schwartz, R. W.; Schneller, T.; Waser, R. Chemical Solution Deposition of Electronic Oxide Films. *C. R. Chim.* **2004**, *7* (5), 433−461.
(39) Develos-Bagarinao, K.; Yamasaki, H.; Nakagawa, Y.; Nie, J. C.; Sohma, M.; Kumagai, T. Comparative Studies of Nanostructural and Morphological Evolution of CeO2 Thin Films Induced by High-Temperature Annealing. *Nanotechnology* **2007**, *18* (16), 165605.
(40) Solovyov, V. F.; Develos-Bagarinao, K.; Nykypanchuk, D. Nanoscale Abnormal Grain Growth in (001) Epitaxial Ceria. *Phys. Rev. B Condens Matter Mater. Phys.* **2009**, *80* (10), 104102.
(41) Coll, M.; Gázquez, J.; Sandiumenge, F.; Puig, T.; Obradors, X.; Espinós, J. P.; Hühne, R. Nanostructural Control in Solution-Derived Epitaxial Ce 1-XGdxO2-y Films. *Nanotechnology* **2008**, *19* (39), 395601.
(42) Campagna, E.; Piperno, L.; Pinto, V.; Augieri, A.; Rufoloni, A.; Mancini, A.; Angrisani Armenio, A.; Masi, A.; Rizzo, F.; Salvato, M.; Celentano, G.; Vannozzi, A.; Rizzo, F.; Celentano, G.; Vannozzi, A. All-Chemical YBCO-Based Architecture Using a Simplified Multilayer Buffer Deposition. *IEEE Trans. Appl. Supercond.* **2022**, *32* (4), 1−5.
(43) Solovyov, V. F.; Ozaki, T.; Atrei, A.; Wu, L.; Al-Mahboob, A.; Sadowski, J. T.; Tong, X.; Nykypanchuk, D.; Li, Q. Highly Efficient Solid State Catalysis by Reconstructed (001) Ceria Surface. *Sci Rep* **2014**, *4*, 4627.
(44) Thornton, J. A. HIGH RATE THICK FILM GROWTH. *Annu. Rev. Mater. Sci.* **1977**, *7* (1), 239−260.
(45) Sandiumenge, F.; Cavallaro, A.; Gàzquez, J.; Puig, T.; Obradors, X.; Arbiol, J.; Freyhardt, H. C. Mechanisms of Nanostructural and Morphological Evolution of CeO2 Functional Films by Chemical Solution Deposition. *Nanotechnology* **2005**, *16*, 1809−1813.
(46) Queraltó, A.; de la Mata, M.; Arbiol, J.; Obradors, X.; Puig, T. Disentangling Epitaxial Growth Mechanisms of Solution Derived Functional Oxide Thin Films. *Adv. Mater. Interfaces* **2016**, *3* (18), 1600392.
(47) Queralto, A.; De La Mata, M.; Arbiol, J.; Hühne, R.; Obradors, X.; Puig, T. Unveiling the Nucleation & Coarsening Mechanisms of Solution-Derived Self-Assembled Epitaxial Ce0.9Gd0.1O2-YNanostructures. *Cryst. Growth Des.* **2017**, *17* (2), 504−516.
(48) Nie, J. C.; Yamasaki, H.; Mawatari, Y. Self-Assembled Growth of CeO2 Nanostructures on Sapphire. *Phys. Rev. B Condens Matter Mater. Phys.* **2004**, *70* (19), 1−11.
(49) Ballabio, G.; Bernasconi, M.; Pietrucci, F.; Serra, S. Ab Initio Study of Yttria-Stabilized Cubic Zirconia Surfaces. *Phys. Rev. B Condens Matter Mater. Phys.* **2004**, *70* (7), 075417.
(50) Qiu, S. R.; Markov, I. Crystal Growth for Beginners. Fundamentals of Nucleation, Crystal Growth and Epitaxy. *World Scientific* **2019**, *75*, 1226.
(51) Dubrovskii, G.; Nucleation, V. *Theory and Growth of Nanostructures*; Springer, 2014.
(52) Noguera, C.; Goniakowski, J.; Finocchi, F.; Freund, H.-J.; Kuhlenbeck, H.; Staemmler, V. *Polar Oxide Surfaces* **2000**, *12*, R367−R410.
(53) Herman, G. S. Characterization of Surface Defects on Epitaxial CeO2(001) Films. *Surf. Sci.* **1999**, *437* (1), 207−214.
(54) Wu, F.; Pavlovska, A.; Smith, D. J.; Culbertson, R. J.; Wilkens, B. J.; Bauer, E. Growth and Structure of Epitaxial CeO2 Films on Yttria-Stabilized ZrO2. *Thin Solid Films* **2008**, *516* (15), 4908−4914.
(55) Jacobsen, S. N.; Helmersson, U.; Erlandsson, R.; Skårman, B.; Wallenberg, L. R. Sharp Microfaceting of (001)-Oriented Cerium Dioxide Thin Films and the Effect of Annealing on Surface Morphology. *Surf. Sci.* **1999**, *429* (1), 22−33.
(56) Seifert, A.; Vojta, A.; Speck, J. S.; Lange, F. F. Microstructural Instability in Single-Crystal Thin Films. *J. Mater. Res.* **1996**, *11* (6), 1470−1481.
(57) Cavallaro, A.; Sandiumenge, F.; Gàzquez, J.; Puig, T.; Obradors, X.; Arbiol, J.; Freyhardt, H. C. Growth Mechanism, Microstructure, and Surface Modification of Nanostructured CeO2 Films by Chemical Solution Deposition. *Adv. Funct. Mater.* **2006**, *16* (10), 1363−1372.
(58) Nolan, M. Charge Compensation and Ce3+ Formation in Trivalent Doping of the CeO2(110) Surface: The Key Role of Dopant Ionic Radius. *J. Phys. Chem. C* **2011**, *115* (14), 6671−6681.
(59) Singh, K.; Kumar, K.; Srivastava, S.; Chowdhury, A. Effect of Rare-Earth Doping in CeO2Matrix: Correlations with Structure, Catalytic and Visible Light Photocatalytic Properties. *Ceram. Int.* **2017**, *43* (18), 17041−17047.
(60) Kumar, S.; Alharthi, F. A.; El marghany, A.; Ahmed, F.; Ahmad, N.; Chae, K. H.; Kumari, K. Role of Fe Doping on Surface Morphology, Electronic Structure and Magnetic Properties of Fe Doped CeO2 Thin Film. *Ceram. Int.* **2021**, *47* (3), 4012−4019.
(61) Katta, L.; Sudarsanam, P.; Thrimurthulu, G.; Reddy, B. M. Doped Nanosized Ceria Solid Solutions for Low Temperature Soot Oxidation: Zirconium versus Lanthanum Promoters. *Appl. Catal., B* **2010**, *101* (1−2), 101−108.
(62) Chen, P. L.; Chen, I. W. Grain Growth in CeO2: Dopant Effects, Defect Mechanism, and Solute Drag. *J. Am. Ceram. Soc.* **1996**, *79* (7), 1793−1800.
(63) Roy, R. Gel Route to Homogeneous Glass Preparation. *J. Am. Ceram. Soc.* **1969**, *52* (6), 344.
(64) Bhuiyan, M. S.; Paranthaman, M.; Salama, K. Solution-Derived Textured Oxide Thin Films - A Review. *Supercond. Sci. Technol.* **2006**, *19* (2), R1−R21.
(65) Capdevila-Cortada, M.; López, N. Entropic Contributions Enhance Polarity Compensation for CeO2(100) Surfaces. *Nat. Mater.* **2017**, *16*, 328−334.
(66) Thompson, C. V. Solid-State Dewetting of Thin Films. *Annu. Rev. Mater. Res.* **2012**, *42*, 399−434.
(67) Mullins, W. W. Theory of Thermal Grooving. *J. Appl. Phys.* **1957**, *28* (3), 333−339.

https://doi.org/10.1021/acs.cgd.5c00172
Cryst. Growth Des. 2025, 25, 3756−3766